

# Three-sensor $3\omega$ - $2\omega$ method for the simultaneous measurement of thermal conductivity and thermal boundary resistance in film-on-substrate heterostructures

Cite as: J. Appl. Phys. **133**, 045104 (2023); <https://doi.org/10.1063/5.0120284>

Submitted: 12 August 2022 • Accepted: 30 December 2022 • Published Online: 27 January 2023

 Guang Yang and  Bing-yang Cao



Journal of Applied Physics **Special Topics** Open for Submissions [Learn More](#)

# Three-sensor $3\omega$ - $2\omega$ method for the simultaneous measurement of thermal conductivity and thermal boundary resistance in film-on-substrate heterostructures

Cite as: J. Appl. Phys. 133, 045104 (2023); doi: 10.1063/5.0120284

Submitted: 12 August 2022 · Accepted: 30 December 2022 ·

Published Online: 27 January 2023




View Online



Export Citation



CrossMark

Guang Yang  and Bing-yang Cao <sup>a)</sup> 

## AFFILIATIONS

Key Laboratory for Thermal Science and Power Engineering of Ministry of Education, Department of Engineering Mechanics, Tsinghua University, Beijing 100084, People's Republic of China

<sup>a)</sup> Author to whom correspondence should be addressed: [caoby@mail.tsinghua.edu.cn](mailto:caoby@mail.tsinghua.edu.cn)

## ABSTRACT

Solid heterostructures composed of substrates and epitaxial films are extensively used in advanced technologies, and their thermophysical properties fundamentally determine the performance, efficiency, and reliability of the corresponding devices. However, an experimental method that is truly appropriate for the thermophysical property measurement of solid heterostructures is still lacking. To this end, a three-sensor  $3\omega$ - $2\omega$  method is proposed, which can simultaneously measure the thermal conductivities of the film and the substrate, along with the film-substrate thermal boundary resistance (TBR) in a single solid heterostructure without any reference samples, showing broad applicability for miscellaneous heterostructures with film thickness ranging from 100 nm to 10  $\mu$ m. In this method, three parallel metal sensors with unequal widths and distances conforming to guidelines for the three-sensor layout design are fabricated on the sample surface, in which the two outer sensors serve as heaters and the middle sensor as a detector. The respective  $3\omega$  signals of the two heaters and the  $2\omega$  signal of the detector are measured, and then the thermophysical properties of the sample are fitted within 3D finite element simulations. To verify this method, two typical wide bandgap semiconductor heterojunctions, i.e., GaN on SiC (#SiC) and GaN on Si (#Si) with  $\sim 2.3 \mu$ m GaN epilayers, are measured. The thermal conductivity of the GaN film, the thermal conductivities of the SiC and Si substrates, and the GaN/substrate TBRs are derived, exhibiting good agreement with the literature. The proposed method will provide a comprehensive solution for the thermophysical property measurements of various solid heterostructures.

Published under an exclusive license by AIP Publishing. <https://doi.org/10.1063/5.0120284>

## I. INTRODUCTION

Solid heterostructures are generally composed of substrates and epitaxial films, and the constituent materials include metals, semiconductors, or insulators. Thanks to their excellent and controllable performance, solid heterostructures have been widely used in power electronics, radio frequency (RF) communications, optoelectronics and photovoltaics, thermoelectricity, and other advanced technology fields.<sup>1–3</sup> Among them, a typical application is the GaN high electron mobility transistor (HEMT), a type of wide bandgap (WBG) semiconductor heterojunction device in power and RF electronics. By growing GaN, AlN, and AlGaIn epitaxial films with a thickness of several micrometers on SiC,

diamond, or other substrates and integrating the wide bandgap characteristics of WBG materials and the high thermal conductivity of the substrate materials, extraordinary electrical performance (high electron mobility, high breakdown voltage, and high power gain, etc.) is finally achieved, with the improvement of the heat dissipation performance to a certain extent.<sup>9</sup> However, with the rapid iteration of device performance, the power density and junction temperature also rise significantly, seriously affecting the device's performance, efficiency, and reliability.<sup>10</sup> Hence, researchers have extensively conducted the thermal analysis and optimization design to cope with these challenges, from the near-junction regions of heterostructure devices to external heat dissipation structures,<sup>11,12</sup> although this is still insufficient for increasingly stringent and

complex thermal management requirements.<sup>13</sup> One of the critical problems points to a high-precision experimental method that is truly appropriate for measuring the thermophysical properties of diverse solid heterostructures.

The typical experimental methods for measuring the thermophysical properties of solid heterostructures contain two main categories: optical and electrical (summarized in Table I). The representative optical methods include the transient thermoreflectance (TTR), the steady-state thermoreflectance (SSTR), the Raman spectroscopy (Raman), and photothermal radiometry (PTR). The electrical methods mainly include the steady-state electrical method, the harmonic method ( $3\omega$  method, etc.), and the scanning thermal microscopy (SThM).

The TTR methods include time-domain thermoreflectance (TDTR) and frequency-domain thermoreflectance (FDTR).<sup>14,15</sup> The laser repeating frequency of TTR is usually on the order of 10 MHz, which makes the thermal penetration depth quite shallow [ $\sim O(100\text{ nm})$ ], resulting in a relatively low signal sensitivity to film-substrate thermal boundary resistance (TBR) for widely used heterostructures with micrometer-scale film thickness. To improve the measurement sensitivity of film-substrate TBR, it is necessary to artificially thin the film to  $\sim O(100\text{ nm})$ .<sup>16</sup> Nonetheless, since the phonons' transport in the film is in the ballistic-diffusion regime,<sup>36</sup> the thinning process inevitably makes the measured results deviate from the properties of the original heterostructures.

To overcome the limitation of the shallow thermal penetration depth, Braun et al.<sup>17</sup> and Song et al.<sup>18</sup> proposed the SSTR method. By significantly reducing the laser frequency to the order of 100 Hz and adjusting the spot size to increase the thermal penetration

depth (up to  $10\text{ }\mu\text{m}$ ), the signal sensitivity to the film-substrate TBR of heterostructures with micrometer-scale film thickness is indeed improved. However, the experiment results show that the method's sensitivity to the substrate thermal conductivity is still unsatisfactory, which makes it necessary to test with the help of bare substrate reference samples.<sup>18</sup>

Raman spectroscopy generally measures local temperature according to the Stokes peak shift.<sup>19</sup> By measuring the internal temperature distribution of a sample and the heating power, the film and substrate thermal conductivities as well as the film-substrate TBR can be derived. The temperature measurement uncertainty of this method is  $\sim 5\text{ K}$ , and the vertical spatial temperature resolution is usually  $>1\text{ }\mu\text{m}$ . These features restrict the measurement precision for the film thermal conductivity and the film-substrate TBR,<sup>20,21</sup> resulting in a rather large TBR uncertainty ( $\sim 10\text{ m}^2\text{ K/GW}$ ),<sup>22</sup> which makes it difficult to satisfy the requirements of high-precision measurement. Additionally, Raman spectroscopy is generally only capable of measuring the thermophysical properties of heterostructures with optically transparent films.<sup>32</sup>

The PTR methods generally include pulsed photothermal radiometry (PPR)<sup>23</sup> and modulated photothermal radiometry (MPR).<sup>24–27</sup> The sample is heated up by the pulsed or continuous wave laser, which is similar to the TTR methods, and the surface temperature oscillation is determined by detecting the IR thermal emission. For the PPR method, the effective thermal conductivity of a thin film with an interface is first fitted from apparent thermal effusivity evolution data, and then the intrinsic film thermal conductivity with the film-substrate TBR can be fitted from the correlation between the effective thermal conductivity and film

TABLE I. Comparison of the main features of existing experimental techniques (T: temperature,  $\kappa_f$ : film thermal conductivity,  $R_I$ : TBR,  $\kappa_{\text{sub}}$ : substrate thermal conductivity,  $t_f$ : film thickness).

Category	Method	Measurability	Accuracy of T	Accuracy of $R_I$	Accuracy of $\kappa_{\text{sub}}$	Requirements	References
Optical	TTR	$\kappa_f, \kappa_{\text{sub}}, R_I$	High	High	Low	$t_f \sim O(100\text{ nm})$ .	14–16
	SSTR	$\kappa_f, R_I$	High	High	Low	Known $\kappa_{\text{sub}}$ or needing reference sample of bare substrate.	17,18
	Raman	$R_I$	Low	Low	Low	Optically transparent film.	19–22
	PTR	$\kappa_f, R_I$ (PPR) $R_I$ (MPR)	High	Moderate (PPR) High (MPR)	Low	(1) Amorphous or disordered film (PPR); (2) Serial samples varying $t_f$ (PPR); (3) Known $\kappa_f$ and $\kappa_{\text{sub}}$ (MPR).	23–27
Electrical	Steady-state	$R_I$	High	Low	Low	N/A	28
	Differential $3\omega$	$\kappa_f, R_I$	Ultra-high	Moderate	Low	(1) Amorphous or disordered film; (2) Serial samples varying $t_f$ ; (3) Known $\kappa_{\text{sub}}$ or needing reference sample of bare substrate.	29–31
	Two-sensor $3\omega-2\omega$	$\kappa_f, \kappa_{\text{sub}}, R_I$	Ultra-high	Moderate	High	(1) Amorphous or disordered film; (2) Serial samples varying $t_f$ .	32
	SThM	$\kappa_f, R_I$	High	Low	Low	(1) Amorphous or disordered film; (2) Serial samples varying $t_f$ ; (3) Needing reference samples with known $\kappa$ for calibration.	33–35
	Three-sensor $3\omega-2\omega$	$\kappa_f, \kappa_{\text{sub}}, R_I$	Ultra-high	High	High	N/A	This work

thickness. There are several limitations of the PPR method. First, it requires the measurement of a series of samples with different film thicknesses to obtain the film thermal conductivity and the film-substrate TBR, which cannot meet the requirement of deriving thermophysical properties within a single sample. Second, it involves the assumption that the film thermal conductivity is independent of the thickness, which means that this method only applies to amorphous or disordered materials.<sup>23</sup> For the MPR method, the amplitude and phase signals of the surface IR thermal emission varying with laser frequency are collected, and a univariant fitting of the film-substrate TBR is performed, since the signals are merely sensitive to the film-substrate TBR in a high-frequency window.<sup>26</sup> However, the film and substrate thermal conductivities are generally referred to the literature, owing to the insufficient sensitivities.<sup>26</sup>

In terms of electrical methods, the steady-state electrical method heats the samples with DC currents,<sup>28</sup> while the harmonic methods ( $3\omega$  method, etc.) are sinusoidal AC heating.<sup>37</sup> Since the thermal penetration depth and the thermal spreading area of steady-state heating are theoretically infinite, the sensor signal of the steady-state method is more sensitive to the thermal contact between the bottom of the entire test sample (consisting of film and substrate) and the sample carrier (e.g., the ceramic dual inline packages, CerDIP), and the error caused by heat radiation cannot be neglected either.<sup>38</sup> These factors will significantly increase the measurement error.

Among all kinds of harmonic methods, the most representative is the differential  $3\omega$  method.<sup>29–31</sup> The temperature oscillations of the heater are measured by the third harmonic of the voltage across the line ( $2\omega$  resistance oscillation times  $1\omega$  driving current), hence the name “ $3\omega$  method.” However, there are three main limitations of this method. First, the method needs to measure a series of samples with varying film thicknesses to extract the film thermal conductivity, which is incapable of deriving thermophysical properties within an individual sample. Second, it is assumed in this method that the film thermal conductivity is independent of the thickness, which restricts this method to measuring amorphous or disordered materials.<sup>29,39</sup> Finally, the fitting intercept of this method includes contributions from the sensor-film TBR, the film-substrate TBR, and the substrate thermal conductivity. Though the substrate thermal conductivity could be substituted from literature or a separate measurement of a bare substrate,<sup>31</sup> it is still challenging to distinguish the sensor-film TBR and the film-substrate TBR, affecting the accuracy of determining film-substrate TBR separately.<sup>32</sup>

To overcome the limitations of the differential  $3\omega$  method, Hua et al. proposed a two-sensor  $3\omega$ - $2\omega$  method,<sup>32</sup> with two parallel sensors (a heater and a detector) fabricated on the sample surface. A current through the heater at frequency  $\omega$  heats the sample at  $2\omega$  and produces the temperature oscillation at frequency  $2\omega$ , which makes the resistance of the heater and detector have a small AC component that oscillates at  $2\omega$ . This resistance oscillation times the AC results in a small voltage oscillation across the heater at  $3\omega$ , while the resistance oscillation times the DC results in a small voltage oscillation across the detector at  $2\omega$ , hence the name “two-sensor  $3\omega$ - $2\omega$  method.” Likewise, this method requires the preparation of a series of heterostructure samples that only change the film thickness to derive the film thermal conductivity, after which the substrate thermal conductivity and the film-

substrate TBR are fitted sequentially. This method still inherits the first two limitations of the differential  $3\omega$  method. Hence, the goal of simultaneous determination of the film and substrate thermal conductivities along with the film-substrate TBR within a single sample cannot be achieved, and this method only applies to materials with thermal conductivity independent of thickness as well.

Scanning thermal microscopy (SThM) is based on a thermally sensitive probe placed on an AFM head,<sup>33</sup> which can operate in passive (sensing) mode or active (heating) mode. The passive-SThM is generally applied for measuring nanoscale in-plane temperature maps, while the active-SThM can further be used to investigate local thermophysical properties by detecting response signals of tip heating. In the active-SThM, heating and sensing with the probe can be performed by the DC or AC mode. The characteristic of SThM is the extremely high spatial resolution ( $\sim 1$  nm) that is capable of mapping the temperature distribution and local thermophysical properties. In terms of measuring the thermophysical properties of a heterostructure, the calibration must be first carried out using several bulk materials of known thermal conductivities that correlate the probe signal with different thermal conductivities. Then, the effective thermal conductivity of the heterostructure sample can be extracted based on the measured signals and the calibration curve. Finally, the intrinsic film thermal conductivity and the film-substrate TBR are fitted from the correlation between the effective thermal conductivity and film thickness.<sup>34,35</sup> As discussed before, it is obvious that the SThM only applies to amorphous or disordered films and cannot meet the requirement of deriving thermophysical properties within an individual sample.

The so-called experimental method that is truly appropriate for measuring thermophysical properties of the solid heterostructures refers to the technique that adapts various heterostructures consisting of films with typical thicknesses (generally 100 nm–10  $\mu$ m) and is able to simultaneously derive the target thermophysical properties (e.g., the film thermal conductivity, the substrate thermal conductivity, and the film-substrate TBR) within a single sample. In addition, it is required that no reference samples be introduced to derive part of the thermophysical properties as known values.

It is not difficult to find that a high-precision experimental method that is truly appropriate for measuring the thermophysical properties of solid heterostructures is still lacking. In this work, the three-sensor  $3\omega$ - $2\omega$  method is proposed, and guidelines for the three-sensor layout design are illustrated. This method is capable of simultaneously measuring the film and substrate thermal conductivities, along with the film-substrate TBR of a solid heterostructure without the need for any reference samples. To verify the accuracy and applicability of this method, two typical WBG heterojunction samples, i.e., GaN on SiC (#SiC) and GaN on Si (#Si), are measured. The GaN thermal conductivity, the substrate thermal conductivity, and the GaN/substrate TBR of these two samples are all within rational ranges in comparison to the literature.

## II. METHOD

### A. Experimental system

As shown in Fig. 1(a), this method mainly measures the thermophysical properties of solid heterostructures composed of films

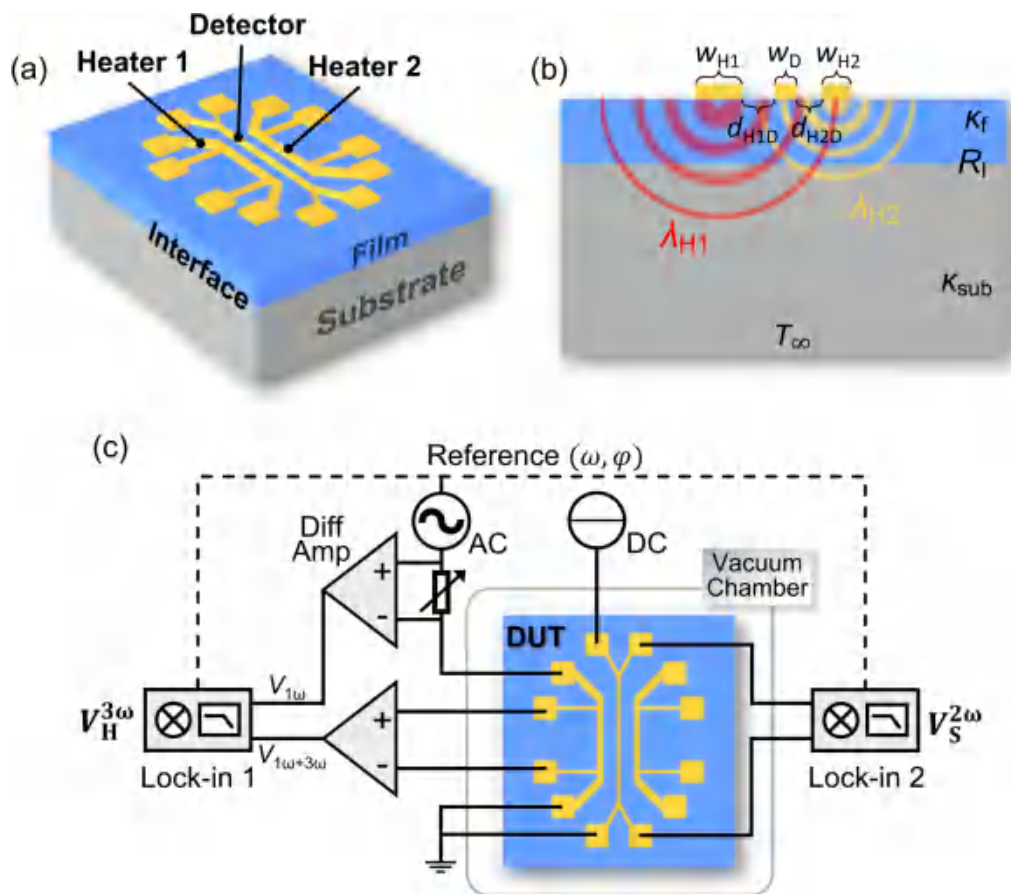


FIG. 1. Typical structure of a test sample (i.e., device under test, DUT) and the experiment system for the three-sensor  $3\omega$ - $2\omega$  method. (a) The heterostructure of the DUT and the three-sensor layout on the surface. (b) The heater heats the sample and the bottom temperature  $T_{\infty}$  is controlled to be constant. The heater width and the heating frequency significantly affect the thermal penetration depth  $\lambda_{H1}$ ,  $\lambda_{H2}$ , which, therefore, affects the sensitivity of the measurement signals. The separable sensitivity to thermophysical properties at different depths (as shown in Fig. S2 in the [supplementary material](#)) makes it possible to derive the film thermal conductivity  $\kappa_f$ , the substrate thermal conductivity  $\kappa_{sub}$ , and the film-substrate TBR  $R_f$  simultaneously in one test. (c) Experiment system and circuit configuration. The heaters (H1 and H2) are energized individually by AC currents instead of synchronously during the test (i.e., H1 on and H2 off; H1 off and H2 on), while the detector (D) is energized by a DC throughout the measurement. The figure illustrates the circuit connection when H1 (or H2) and D are working synchronously.

and substrates. An insulating layer deposited on the film surface is required to prevent leakage and crosstalk between sensors, except for well-insulating film materials. Then three parallel metal sensors with optimized widths and distances are fabricated on the surface by lithography, sputtering, and lift-off processes successively. The two outer sensors are heaters, among which the wider one is denoted as Heater 1 (H1), and the narrower one Heater 2 (H2). The middle sensor is used as a Detector (D), thus forming an effective sample (i.e., device under test, DUT). The guidelines for the three-sensor layout design are discussed in Sec. II D.

Figure 1(b) shows the five characteristic geometry parameters that need to be carefully designed for the three-sensor layout: H1 width  $w_{H1}$ , H2 width  $w_{H2}$ , D width  $w_D$ , H1-D distance  $d_{H1D}$ , and H2-D distance  $d_{H2D}$ . In addition, Fig. 1(b) also illustrates the relationship between the thermal penetration depth  $\lambda_{H1}$ ,  $\lambda_{H2}$  (where

the temperature oscillation amplitude is  $1/e$  of that at the heat source<sup>37</sup>) and the film thickness. By adjusting the heater width and the heating frequency, the thermal penetration depth can be controlled,<sup>22,29</sup> so the signal sensitivity of each sensor to the thermophysical properties at different depths is separable (as shown in Fig. S2 in the [supplementary material](#)). Therefore, it is possible to derive the film thermal conductivity  $\kappa_f$ , the substrate thermal conductivity  $\kappa_{sub}$ , and the film-substrate thermal boundary resistance (TBR)  $R_f$  simultaneously in a single sample.

Based on the three-sensor layout of the DUT shown in Figs. 1(a) and 1(b), the experimental system is set up as shown in Fig. 1(c). First, the DUT is assembled in a vacuum chamber to avoid the introduction of errors by convection and radiation and to ensure accurate temperature control. The three sensors are connected to the external circuit through a wire-bonding process, and

the switching sequence of these two heaters is asynchronous. Specifically, the heater H1 is first energized individually by an AC current source (e.g., Keithley 6221) with the H2 power-off, while the detector D is powered by a DC current source (e.g., Keithley 2450). And then, the H2 is energized individually by an AC current with the H1 power-off, while the detector D is continuously powered by a DC current.

The temperature oscillations of the heater are measured by the third harmonic of the voltage across the heater, while the temperature oscillations of the detector (near the heater) are measured by the second harmonic of the voltage, hence the name “ $3\omega$ - $2\omega$  method.” An AC current through the heater at frequency  $\omega$  heats the sample at  $2\omega$  and produces the temperature oscillation at frequency  $2\omega$ , which makes the resistance of the heater and detector contain an AC component that oscillates at  $2\omega$ . This resistance oscillation times the  $1\omega$  driving current results in a small  $3\omega$  voltage oscillation across the heater, while the resistance oscillation times the DC current results in a small  $2\omega$  voltage oscillation across the detector. The heater’s  $3\omega$  signal and the detector’s  $2\omega$  signal are collected by two lock-in amplifiers (e.g., SRS SR830), respectively, with the reference frequency and phase of each lock-in amplifier provided by the AC current source.

It should be noticed that the three-sensor  $3\omega$ - $2\omega$  method proposed in this work is an improved generation of the previously reported two-sensor  $3\omega$ - $2\omega$  method,<sup>32</sup> and the detailed comparison between these two methods is discussed in Sec. S1 in the [supplementary material](#).

Moreover, owing to the limitation of the lock-in amplifier’s dynamic reserve, it is necessary to connect a variable resistor with the same resistance as the heater in series before the heater. Then, signals of the heater and the variable resistor are input into the lock-in amplifier under the differential mode, thereby subtracting

the  $1\omega$  common-mode voltage signal, which is done to prevent the lock-in amplifier from overloading.<sup>40</sup>

## B. Measurement procedure

Consistent with the experiment system presented in Sec. II A, an illustrative experimental procedure is proposed (Fig. 2), which in principle achieves the simultaneous measurement of the equivalent thermal conductivity of the insulating layer  $\kappa_{\text{ins}}$ , the film thermal conductivity  $\kappa_f$ , the substrate thermal conductivity  $\kappa_{\text{sub}}$ , and the film-substrate TBR  $R_f$  within a single heterostructure DUT. Three factors contribute to  $\kappa_{\text{ins}}$ : the sensor-insulating layer TBR, the thermal resistance of the insulating layer itself, and the insulating layer-film TBR. The basic concept of this method is to determine the target thermophysical properties with the inverse problem method (fitting algorithms) based on the three-dimensional finite element modeling (FEM).

However, a local minimum trap is inevitable if we directly fit all four undetermined parameters ( $\kappa_{\text{ins}}$ ,  $\kappa_f$ ,  $\kappa_{\text{sub}}$ , and  $R_f$ ) simultaneously. One of the viable strategies to avoid a local minimum trap in the optimization algorithm may be to split a multi-parameter fitting problem into several univariate fitting problems. Fortunately, this is feasible with the optimized three-sensor layout design (conforming to guidelines in Sec. II D). More details about how the fitting is performed to determine the four parameters ( $\kappa_{\text{ins}}$ ,  $\kappa_f$ ,  $\kappa_{\text{sub}}$ , and  $R_f$ ), respectively, are illustrated in Sec. S2 in the [supplementary material](#). The key operations after the preparation stage shown in Fig. 2 are the following three steps, i.e., the “three-step” routine based on separable sensitivities of different thermophysical properties.

- (1) The AC current ( $I_{H1}$ ) is connected to the wider heater H1 individually, while the DC current ( $I_{D1}$ ) is connected to detector

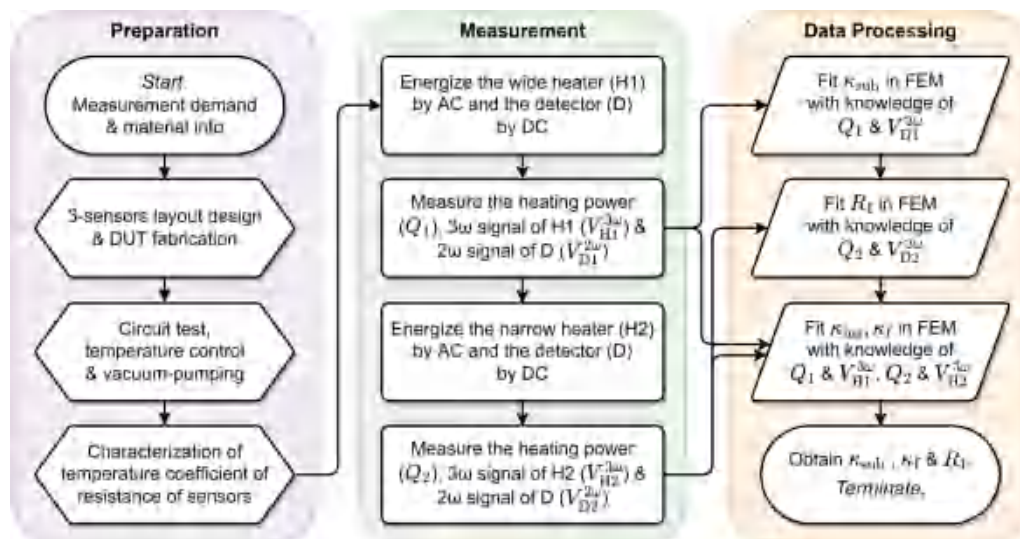


FIG. 2. Measurement procedure of the three-sensor  $3\omega$ - $2\omega$  method. The data processing stage is a “three-step” routine based on separable sensitivities of different thermophysical properties.

D. Measure the heating power ( $Q_1$ ), the  $3\omega$  signal of H1 ( $V_{H1}^{3\omega}$ ), and the  $2\omega$  signal of D ( $V_{D1}^{2\omega}$ ). Based on  $Q_1$  and  $V_{D1}^{2\omega}$ , the substrate thermal conductivity  $\kappa_{\text{sub}}$  is fitted by solving the inverse problem in FEM. Optimization algorithms (Levenberg–Marquardt algorithm,<sup>41</sup> etc.) are applied to minimize the deviation of the sensors’ thermal responses between the lock-in amplifiers’ readouts with the FEM results, and then the best-fit is drawn in correspondence to the undetermined thermophysical properties.

- (2) The AC current ( $I_{H2}$ ) is connected to the narrower heater H2 individually, while the DC current ( $I_{D2}$ ) is connected to detector D. The heating power ( $Q_2$ ), the  $3\omega$  signal of H2 ( $V_{H2}^{3\omega}$ ), and the  $2\omega$  signal of D ( $V_{D2}^{2\omega}$ ) are measured. Based on  $Q_2$ ,  $V_{D2}^{2\omega}$ , and the  $\kappa_{\text{sub}}$  obtained in the first step, the film-substrate TBR  $R_I$  is fitted.
- (3) Based on  $Q_1$  and  $V_{H1}^{3\omega}$ ,  $Q_2$  and  $V_{H2}^{3\omega}$ , along with the obtained  $\kappa_{\text{sub}}$  and  $R_I$ , the equivalent thermal conductivity of the insulating layer  $\kappa_{\text{ins}}$  and the film thermal conductivity  $\kappa_f$  are simultaneously fitted.

Additionally, the amplitude of each sensor’s signal is mainly utilized throughout this method due to the relatively larger error of the phase. It should be noted that the above experimental procedure is flexible. In principle, the sequential order for deriving  $\kappa_{\text{ins}}$ ,  $\kappa_f$ ,  $\kappa_{\text{sub}}$ , and  $R_I$  and which sensor signal is adopted are determined by the sensitivity analysis. This varies with the DUT’s practical structure and material, so the derivation process of the thermophysical properties should be adapted to the actual situation, which is discussed in Secs. S3 and S4 in the [supplementary material](#).

### C. Model and signals

As mentioned in Sec. II A, the work mode of the two heaters is sequential (individually heating) instead of synchronous (simultaneously heating) during the experiment, while the detector is working continuously during each heater heating the sample, so there are only one heater and one detector working simultaneously

in this method. To clearly analyze the test signal, the DUT model composed of the two parallel sensors shown in Fig. 3 is considered.

The DUT model consists of the material under test and two adjacent parallel metal sensors on the surface. It is consistent with the typical  $3\omega$  method<sup>37</sup> that AC current  $I(t) = I_H \cos(\omega t)$  is applied to the heater. The metal sensor can be regarded as a pure resistance  $R^{\text{el}}$ , whose inductance and capacitance can be neglected at a non-high frequency. Under this condition, the heating power is the superposition of the steady-state heat source  $Q^{\text{st}}$  ( $\frac{1}{4} I_H^2 R_{H0}^{\text{el}}$ ) and the harmonic heat source  $Q^{2\omega}$  ( $\frac{1}{2} I_H^2 R_{H0}^{\text{el}} \cos(2\omega t)$ ) with a frequency of  $2\omega$ ,

$$Q(t) = \frac{1}{4} I(t)^2 R_{H0}^{\text{el}} = \frac{1}{4} I_H^2 R_{H0}^{\text{el}} [1 + \cos(2\omega t)] \quad (1)$$

$R_{H0}^{\text{el}}$  represents the heater’s electrical resistance at the reference temperature. In addition, the DUT shown in Fig. 3 [and Fig. 1(a)] can be regarded as a linear thermal impedance device.<sup>29,42,43</sup> Thus, the thermal response signal  $\theta$  (i.e., the temperature change) can be directly decomposed into two components corresponding to the heat sources in Eq. (1): the steady-state temperature rise  $\theta^{\text{st}}$  associated with the steady-state heat source  $Q^{\text{st}}$ , and the temperature oscillation  $\theta^{2\omega}$  associated with the harmonic heat source  $Q^{2\omega}$ .<sup>29</sup> Then, the thermal responses of the heater and detector can be denoted as

$$\begin{cases} \theta_H = \frac{1}{4} \theta_H^{\text{st}} + \theta_H^{2\omega} \cos(2\omega t + w), \\ \theta_D = \frac{1}{4} \theta_D^{\text{st}} + \theta_D^{2\omega} \cos(2\omega t + \psi). \end{cases} \quad (2a; 2b)$$

The phase  $w$  of the heater thermal response reflects the time delay caused by the heat capacity of the heater itself and the sample, while the  $\psi$  of the detector reflects the influence of the heat capacity and the distance between the detector and heater.<sup>44</sup> In addition, when the temperature change is small, there is a good linear relationship between the metal electrical resistance and the temperature, which can be characterized by the temperature coefficient of the electrical resistance (TCR, denoted by  $\beta = \frac{1}{R_0} \frac{\partial R^{\text{el}}}{\partial T}$ ,  $R^{\text{el}} = R_0^{\text{el}}(1 + \beta\theta)$ ).<sup>42,45,46</sup> Hence, the resistance changes of the

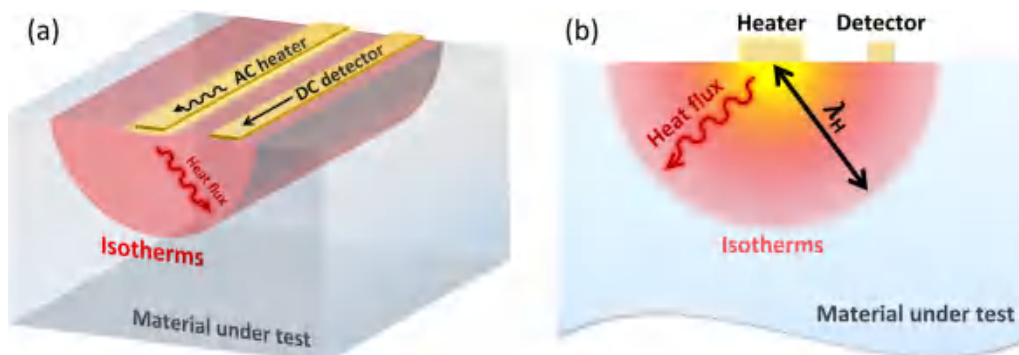


FIG. 3. An illustrative two-sensor DUT model. (a) Schematic of the heat flux and temperature oscillation amplitude inside the sample when the heater is connected to AC and the detector is connected to DC. The isotherm is the isosurface of temperature amplitude  $\theta^{2\omega}$ , excluding the steady-state temperature rise component  $\theta^{\text{st}}$ . The DC current is usually small, so the heat flux generated by the detector is negligible. (b) Schematic of the thermal penetration depth  $\lambda_H$  of the harmonic heat source  $Q^{2\omega}$ .

heater and the detector due to temperature changes are denoted as follows:

$$\begin{cases} R_H^{el} \approx R_{H0}^{el} [1 \pm \beta_H \theta_H^{st} \pm \beta_H \theta_H^{2\omega} \cos(2\omega t \pm \psi)], \\ R_D^{el} \approx R_{D0}^{el} [1 \pm \beta_D \theta_D^{st} \pm \beta_D \theta_D^{2\omega} \cos(2\omega t \pm \psi)]. \end{cases} \quad (3a; 3b)$$

A sinusoidal AC current at  $1\omega$  frequency and the resistance change at  $2\omega$  frequency result in a  $3\omega$  component in the voltage signal on the heater,<sup>47</sup>

$$V_H(t) \approx I_H R_{H0}^{el} \begin{bmatrix} (1 \pm \beta_H \theta_H^{st}) \cos(\omega t) \pm \frac{1}{2} \beta_H \theta_H^{2\omega} \cos(\omega t \pm \psi) \\ \pm \frac{1}{2} \beta_H \theta_H^{2\omega} \cos(3\omega t \pm \psi) \end{bmatrix} \quad (4)$$

Meanwhile, a constant DC current  $I_D$  is connected to the detector. The constant DC current and the resistance change of the  $2\omega$  frequency cause the voltage signal on the detector to contain a  $2\omega$  component,

$$V_D(t) \approx I_D R_{D0}^{el} [1 \pm \beta_D \theta_D^{st} \pm \beta_D \theta_D^{2\omega} \cos(2\omega t \pm \psi)] \quad (5)$$

Figure 4 summarizes and laterally compares the current, temperature oscillation, resistance change, and voltage response waveforms of the heater and the detector. It is obvious in Eqs. (4) and (5) that the  $3\omega$  component  $V_H^{3\omega}$  of the heater voltage signal and the  $2\omega$  component  $V_D^{2\omega}$  of the detector voltage signal are both

linearly related to the temperature oscillation  $\theta^{2\omega}$ ,<sup>37,45,48</sup> i.e.,

$$\begin{cases} \theta_H^{2\omega} \approx \frac{2 V_H^{3\omega, rms}}{I_H^{rms} R_{H0}^{el} \beta_H}, \\ \theta_D^{2\omega} \approx \frac{2 V_D^{2\omega, rms}}{I_D R_{D0}^{el} \beta_D}. \end{cases} \quad (6a; 6b)$$

Therefore, by detecting the RMS values of  $V_H^{3\omega}$  and  $V_D^{2\omega}$  through the lock-in amplifiers, the temperature oscillation on each sensor can be directly obtained using Eq. (6), whose amplitude and phase contain the thermophysical properties of the DUT.

In addition, the  $I_D$  also generates an additional steady-state temperature rise  $\theta^0$  on the sample, the heater, and the detector. However, since  $I_D$  is generally small and the steady-state temperature rise  $\theta^0$  does not affect the  $3\omega$  signal of the heater and the  $2\omega$  signal of the detector,  $\theta^0$  can, therefore, be neglected in principle.

#### D. Guidelines for the three-sensor layout design

In Sec. II B, we have indicated that the solution to prevent a local minimum trap is to split a multi-parameter fitting problem into several univariate fitting problems, and the prerequisite for this strategy is the optimized three-sensor layout design. The guidelines for optimizing the layout design are elaborated on in this section.

The foundation of the mentioned strategy and the “three-step” routine is to engineer several possible geometric designs of the “heater-detector” group, and each geometric design should distinguish the signal sensitivity of an individual thermophysical property ( $\kappa_{ins}$ ,  $\kappa_f$ ,  $\kappa_{sub}$ , or  $R_l$ ) from the others. For example, if one is dedicated to extract the substrate thermal conductivity  $\kappa_{sub}$ , the

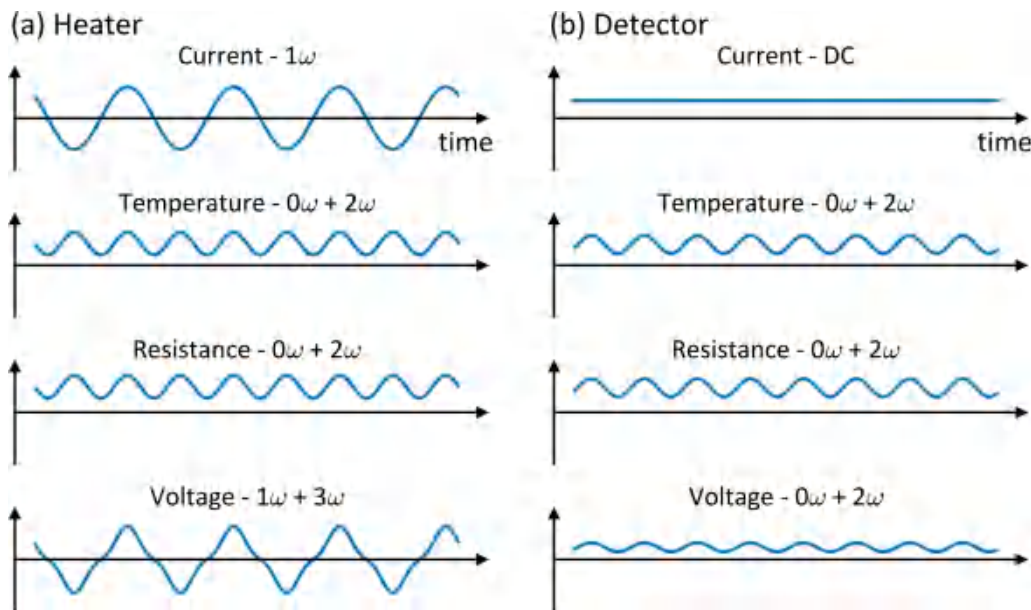


FIG. 4. Schematic of waveforms of the applied current, temperature oscillation, resistance change, and voltage response on each sensor. (a) Heater; (b) detector.



corresponding geometric dimensions of the heater and detector should be carefully designed for the purpose of improving the signal sensitivity to  $\kappa_{\text{sub}}$  and limiting the sensitivity to  $\kappa_{\text{ins}}$ ,  $\kappa_f$ , and  $R_f$ .

The layout design is determined by three characteristic geometric parameters: the heater width  $w_H$ , the heater-detector distance  $d_{\text{HD}}$ , and the detector width  $w_D$ . Thus, based on the detailed sensitivity analysis of sensors' signals and the resulting four feasible regions (Sec. S3 in [supplementary material](#)), guidelines for the three-sensor layout design are summarized as follows.

- (1) To determine  $\kappa_{\text{sub}}$ : A wide heater H1 is arranged on the upper surface of the sample, and a narrow detector D1 is located at a relatively long distance from H1. Under this condition, the  $2\omega$  signal on D1 is merely sensitive to  $\kappa_{\text{sub}}$  with H1 individually heating the sample.
- (2) To determine  $R_f$ : A narrow heater H2 is arranged, and a narrow detector D2 is in the vicinity. This group of sensors is used to derive  $R_f$  based on the measured  $\kappa_{\text{sub}}$ . Under this condition, the  $2\omega$  signal on D1 is sensitive to both  $\kappa_{\text{sub}}$  and  $R_f$  with H2 individually heating the sample.
- (3) To determine  $\kappa_{\text{ins}}$  and  $\kappa_f$ : The signals of the wide heater H1 and the narrow heater H2 are synthesized to derive  $\kappa_{\text{ins}}$  and  $\kappa_f$  simultaneously based on the  $\kappa_{\text{sub}}$  and  $R_f$  measured in the preceding two steps. The  $3\omega$  signal across H1(H2) are sensitive to both  $\kappa_{\text{ins}}$  and  $\kappa_f$  with H1(H2) heating the sample.
- (4) Simplify layout design: D1 and D2 can be merged into a single detector D to simplify the sensor layout without affecting the measurement precision. Thus, the three-sensor layout consisting of a wide heater H1, a narrow heater H2, and a detector D is designed (as illustrated in Sec. II A).

The foregoing guidelines are especially appropriate for the typical GaN on SiC heterostructure discussed in Sec. S3 in the [supplementary material](#). In practice, the layout design should be adapted to the actual sensitivity analysis results of a specific sample, which generally vary with the consisting material and stacking structure (as demonstrated in Sec. S4 in the [supplementary material](#)).

### III. RESULTS AND DISCUSSION

To verify the validity and the accuracy of the proposed three-sensor  $3\omega$ - $2\omega$  method, two kinds of typical heterojunctions, i.e., GaN on SiC (#SiC, 4H-SiC substrate with GaN film) and GaN on Si (#Si, undoped Si substrate with GaN film), are measured at 300 K. Both samples are prepared using the metal organic chemical vapor deposition (MOCVD) process with annealing.

For sample #SiC, an AlN nucleation layer with an  $\sim 40$  nm thickness is first grown on a  $90\ \mu\text{m}$  4H-SiC substrate to buffer the stress caused by the lattice and thermal expansion mismatch between the GaN film and the substrate, improving the epitaxial quality of GaN. Then an  $\sim 2.3\ \mu\text{m}$  GaN epilayer is sequentially grown on AlN to form a GaN/AlN/SiC "sandwich" structure. For sample #Si, an  $\sim 300$  nm AlN nucleation layer is grown on a  $95\ \mu\text{m}$  undoped Si(111) substrate, and then an  $\sim 2.3\ \mu\text{m}$  GaN epitaxial layer is grown on AlN to form a GaN/AlN/Si "sandwich" structure. The significant difference in the nucleation layer thickness is

attributed to the much more serious lattice and thermal expansion coefficient mismatch between Si and GaN than that of SiC.<sup>49,50</sup> To improve the lattice quality of the GaN epilayer of sample #Si, the AlN thickness needs to be increased. Owing to the existence of the AlN nucleation layer, the film-substrate thermal boundary resistance (TBR)  $R_f$  measured in this study is actually the superposition of three factors, including the GaN/AlN TBR, the thermal resistance of the AlN nucleation layer, and the AlN/substrate TBR.

To avoid the leakage current and suppress the crosstalk between sensors, a  $\text{SiO}_2$  insulating layer of  $\sim 40$  nm is deposited on the GaN layer with the plasma enhanced chemical vapor deposition (PECVD) process, and then a complete heterostructure sample is formed. The layered structures of both samples are characterized by a transmission electron microscope (TEM) as shown in [Figs. 5\(a\) and 5\(b\)](#). It is obvious that there are more dislocation cores near the AlN/Si interface [black dots shown in [Fig. 5\(b\)](#)] of #Si, which ascribes to the more serious lattice mismatch between Si and AlN. Then the corresponding three-sensor layouts are fabricated on the  $\text{SiO}_2$  upper surface of the two samples via lithography, sputtering, and lift-off processes successively, and complete DUTs are finally formed.<sup>32</sup> The material of sensors in this study is 90 nm Au/10 nm Cr (Cr for adhesion), and the actual sensor morphology is shown in [Figs. 5\(c\) and 5\(d\)](#). The three-sensor layout is designed based on the guidelines demonstrated in Sec. II D. For both samples, the specific sensor dimensions are measured with the scanning electron microscope (SEM), respectively ([Table II](#)). The measurement details are shown in Sec. S5 in the [supplementary material](#).

According to the experimental procedure illustrated in [Fig. 2](#), after the DUT fabrication and the experimental circuit test, each sensor's temperature coefficient of electrical resistance (TCR) needs to be calibrated first. The calibration results show that the TCRs for each sensor on the two samples are close ( $\sim 1.8 \times 10^{-3}/\text{K}$  near 300 K, see Sec. S6 in [supplementary material](#)), which is ascribed to each metal sensor consisting of the same material.

Next, AC currents are applied to heaters H1 or H2 sequentially of each sample, and a constant DC current is applied to the detector D while H1 or H2 is heating. Then the heating power is adjusted and the trend of the thermal response  $\theta^{2\omega}$  of each sensor is recorded. The results are shown in [Fig. 6](#), in which the scattered points are the raw data, and the error bars of data points are so small that they are covered by the points. The straight lines correspond to the best-fit thermophysical properties combinations ( $\kappa_{\text{ins}}$ ,  $\kappa_f$ ,  $\kappa_{\text{sub}}$ , and  $R_f$ ), which are obtained by solving the inverse problem based on the Levenberg-Marquardt algorithm<sup>41</sup> within the 3D FEM simulation (the fitting procedure is in line with that in Sec. S2 in the [supplementary material](#)). It is obvious that there is an excellent linear relationship between the thermal response  $\theta^{2\omega}$  of each sensor and the heating power, which verifies the fact that both samples can be regarded as linear thermal impedance devices and validates the high precision of the measurement.

The final measurement results at room temperature (300 K) are listed in [Table III](#), and the error analyses are given in Sec. S7 in the [supplementary material](#). To examine the robustness of our results obtained from the fitting algorithm, we use several initial guesses and verify that the fitting routines converge to the same set of best-fit values.<sup>15</sup> For sample #SiC, the GaN film's thermal conductivity is  $167.9 \pm 7.4$  W/mK, and the SiC substrate's thermal

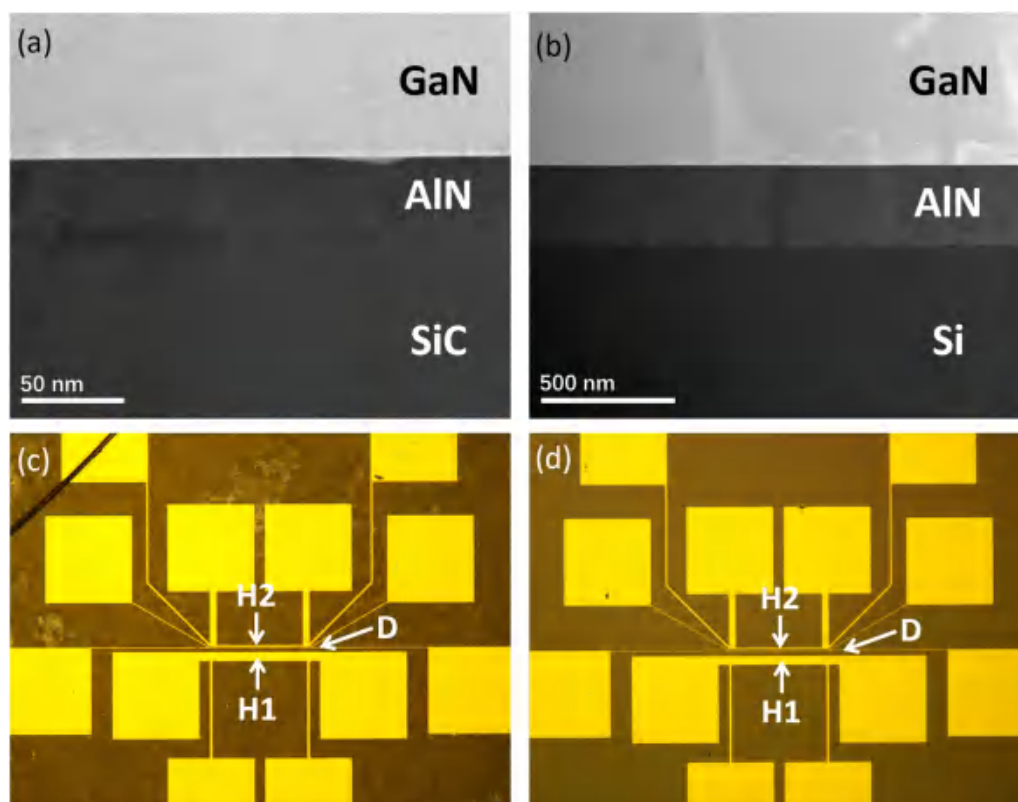


FIG. 5. The “sandwich” structure and the three-sensor morphology of each sample. (a) GaN/AlN/SiC “sandwich” structure of sample #SiC, (b) GaN/AlN/Si “sandwich” structure of sample #Si. There are more dislocation cores (black dots) near the AlN/Si interface of #Si. The actual three-sensor layout of (c) sample #SiC and (d) sample #Si.

conductivity is  $389.1 \pm 9.6$  W/m K. For #Si, the GaN film’s thermal conductivity is  $165.4 \pm 10.2$  W/m K, and the Si substrate’s thermal conductivity is  $147.2 \pm 3.7$  W/m K. The thermal conductivities of the GaN films for both samples are close, and all the thermal conductivity measurements discussed above are in good agreement with the reported data in the literature.<sup>19,49,51–54</sup>

For thermal boundary resistance, the GaN/SiC TBR of sample #SiC is measured to be  $5.1 \pm 1.0$  m<sup>2</sup> K/GW, while the GaN/Si TBR of sample #Si is  $11.7 \pm 2.1$  m<sup>2</sup> K/GW. The GaN/SiC TBR is relatively lower than that for GaN/Si, which may be ascribed to two factors. First, the matching of the lattice constant and the thermal expansion coefficient between SiC, GaN, and AlN is better than that of the Si substrate, which results in a higher lattice quality near the AlN/SiC interface of the #SiC, with fewer lattice defects and

dislocation cores [as shown in Figs. 5(a) and 5(b)]. Therefore, the scattering rate of phonons near the nucleation layer in the #SiC is smaller than that of the #Si in principle. Second, the defect density in the AlN nucleation layer is extremely high (atomic vacancy density  $>10^{21}$  cm<sup>-3</sup>),<sup>19,49,50,55</sup> and the thickness of AlN is thin, so the phonons scattering by the defect and boundary in this layer are significant, resulting in the thermal conductivity of AlN (generally  $<25$  W/m K<sup>52</sup>) being much lower than the bulk value. Although the increase in the AlN layer thickness can reduce phonon boundary scattering rate and somewhat improve the thermal conductivity, it is still not enough to offset the increase in total thermal resistance caused by the increasing thickness. Thus, the thicker AlN layer is responsible for the larger TBR of sample #Si as well.

The TBR measurement results in this work are compared with representative studies in the literature, as shown in Table IV and Fig. 7. For sample #SiC, the TBR result in this study is quite consistent with that of the MOCVD sample with an  $\sim 36$  nm AlN nucleation layer prepared by Cho et al.<sup>49</sup> Moreover, our result is slightly higher than those of the annealed samples with no nucleation layer prepared by Mu et al.<sup>54</sup> using a surface activated bonding process [SAB(A)] and the samples with no nucleation layer prepared by Ziade et al.<sup>53</sup> via the molecular beam epitaxy (MBE) process. In

TABLE II. Specific dimensions of each sensor on both samples (units:  $\mu\text{m}$ ).

Sample	$w_{H1}$	$w_{H2}$	$w_D$	$d_{H1D}$	$d_{H2D}$
#SiC	42.50	7.741	4.689	17.19	2.233
#Si	42.95	8.113	4.987	21.81	2.754

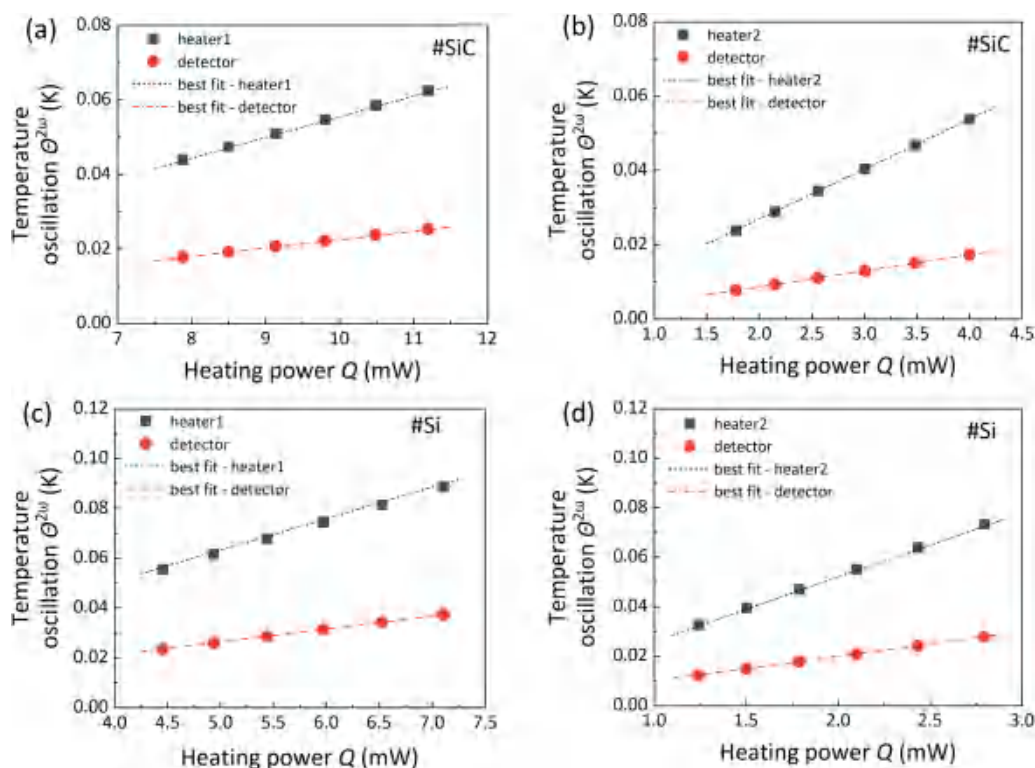


FIG. 6. Measurements of the two samples. Sample #SiC: (a) Thermal response signals of H1 and D during H1 individually heating, (b) thermal response signals of H2 and D during H2 individually heating. Sample #Si: (c) thermal response signals of H1 and D during H1 individually heating and (d) thermal response signals of H2 and D during H2 individually heating. The scattered points are the raw data, and the straight lines are the best-fit lines corresponding to the optimal thermophysical property combinations obtained by solving the inverse problem based on 3D FEM simulation.

addition, the TBR of the #SiC is slightly lower than that of the unannealed samples (SAB) prepared by Mu et al.<sup>54</sup> and is significantly lower than that of the MOCVD sample with an  $\sim 70$  nm AlN nucleation layer prepared by Manoi et al.<sup>56</sup>

Among the aforementioned fabrication processes, the MBE process generally produces heterostructures with the highest quality interface characterized by atomic level flatness and few defects. Moreover, since the temperature in the MBE process is relatively low (700–800 °C), the influence of the thermal expansion coefficient mismatch is small, and the atom diffusion near the interface is weak.<sup>57–59</sup> Therefore, for materials with good lattice matching such as GaN and SiC, the MBE process can directly grow the GaN epilayer on a SiC substrate without introducing additional AlN transition layers. Hence, the TBR of heterostructures prepared with MBE is generally low.

TABLE III. Measured thermophysical properties of the two samples at 300 K.

Sample	$\kappa_{\text{GaN}}$ (W/m K)	$\kappa_{\text{sub}}$ (W/m K)	$R_1$ ( $\text{m}^2$ K/GW)
#SiC	$167.9 \pm 7.4$	$389.1 \pm 9.6$	$5.1 \pm 1.0$
#Si	$165.4 \pm 10.2$	$147.2 \pm 3.7$	$11.7 \pm 2.1$

In terms of the SAB technique, the bonding surfaces of the GaN and SiC need to be bombarded with Ar ion beams to activate the surfaces before the bonding process, leading to the formation of a nanometer-thick amorphous layer near the bombarded surfaces, and then the GaN and SiC are bonded together. After the bonding process is completed, an amorphous layer with a thickness of 3–5 nm remains near the interface.<sup>54</sup> Owing to the extremely low thermal conductivity of the amorphous materials (generally  $<2$  W/m K at room temperature), the TBR is generally higher than that of the MBE samples. To improve the interface quality of the SAB samples, post-processing such as high-temperature annealing is beneficial. After annealing, the amorphous areas near the interface are significantly reduced, replaced by polycrystalline structures and dislocations after high-temperature recrystallization.<sup>54</sup> Thus, the interface morphology and the TBR after annealing are close to those of the MBE samples.

MOCVD is a mature process that is widely used in the fabrication of semiconductor heterostructures, and the temperature in the MOCVD process is higher (up to 1100 °C)<sup>60</sup> compared with MBE and SAB. Accordingly, in addition to lattice matching, the thermal expansion coefficient mismatch is not negligible, and an additional nucleation layer between the substrate and the epilayer is necessary to buffer the stress during epitaxial growth. Although the

TABLE IV. Representative TBR measurements in literature (300 K) (NL: nucleation layer).

Substrate	Study	Method	NL	Growth	$R_t$ ( $m^2$ K/GW)
SiC	This work	$3\omega$ - $2\omega$	40 nm AlN	MOCVD	$5.1 \pm 1.0$
	Mu et al. <sup>54</sup>	TDTR	No	SAB	$5.9 + 0.7/-0.5$
				SAB and anneal	$4.4 + 1.3/-0.8$
	Ziade et al. <sup>53</sup>	FDTR	No	MBE	$4.3 + 0.5/-0.4$
	Cho et al. <sup>49</sup>	TDTR	36 nm AlN	MOCVD	$5.3 \pm 1.3$
	Manoi et al. <sup>56</sup>	Raman	70 nm AlN	MOCVD	$20.1 \pm 5.0$
Si	This work	$3\omega$ - $2\omega$	300 nm AlN	MOCVD	$11.7 \pm 2.1$
	Bougher et al. <sup>52</sup>	TDTR	100 nm AlN	MOCVD	$7.0 \pm 1.7$
	Cho et al. <sup>49</sup>	TDTR	38 nm AlN	MBE	$7.8 \pm 1.2$

nucleation layer is helpful, the lattice defects and dislocations in the nucleation layer are still dense, while the atom diffusion and amorphous areas near the interface are still obvious. Hence, the TBR of the MOCVD sample is generally higher than that of the MBE sample and the annealed SAB sample. In the previous studies, Cho et al.'s sample structure and growth process<sup>49</sup> are very similar to those in this study, and the measured TBR value is likewise close to that of this study. Furthermore, MOCVD is widely used in large-scale production, and the growth rate is adjusted in a wide range by controlling the gas flow rate of the reaction source, which inevitably results in large deviations in the growth quality of MOCVD samples provided by different suppliers.<sup>56</sup> Hence, it is understandable that the TBR result of the MOCVD sample prepared by Manoi et al.<sup>56</sup> is quite different from others.

For sample #Si, the TBR result is higher than that of the MBE sample with an  $\sim 38$  nm AlN nucleation layer fabricated by Cho et al.<sup>49</sup> and the MOCVD sample with an  $\sim 100$  nm AlN nucleation layer prepared by Bougher et al.<sup>52</sup> This deviation is mainly ascribed

to the much thicker AlN nucleation layer of the sample #Si, which increases the equivalent thermal boundary resistance due to its reduced thermal conductivity.<sup>52</sup> If the excess AlN thickness in sample #Si is subtracted, a TBR value closer to Cho et al.'s<sup>49</sup> and Bougher et al.'s<sup>52</sup> can be obtained.

In addition, the TBR results are compared to DMM model predictions.<sup>22</sup> As shown in Fig. 7, the GaN/SiC TBR predicted by the DMM model is  $\sim 1.1 m^2$  K/GW, with the GaN/Si TBR being  $\sim 0.8 m^2$  K/GW, which are both significantly lower than the experimental value. Generally, the DMM model underestimates the TBR significantly,<sup>22,32</sup> since DMM only considers the mismatch of the phonon DOS and group velocity inside the material on both sides of the interface, ignoring the anharmonic effect, the interfacial localized phonon modes, and the scattering effects of dense defects near the interface. Moreover, the additional thermal resistance corresponding to the nucleation layer introduced in practical heterostructures is absent in the DMM model as well.

In summary, the measurement results given by the proposed three-sensor  $3\omega$ - $2\omega$  method are all consistent with the existing representative studies in the literature, which verifies the method's accuracy, reliability, and applicability to the thermophysical property measurements of typical heterostructures with film thicknesses of several micrometers.

#### IV. CONCLUSIONS

A three-sensor  $3\omega$ - $2\omega$  method is proposed in this study, which can simultaneously measure thermal conductivities of the film and the substrate, along with the film-substrate thermal boundary resistance (TBR) within a single heterostructure sample, exhibiting broad applicability for heterostructures with film thicknesses ranging from 100 nm to 10  $\mu$ m. In this method, three parallel metal sensors with unequal widths and distances conforming to the guidelines for three-sensor layout design are fabricated on the sample surface. The two outer sensors are used as heaters, and the middle sensor is used as a detector. By measuring the respective  $3\omega$  signals of the two heaters and the  $2\omega$  signal of the detector and then solving the inverse problem based on the 3D finite element simulation, the film and substrate thermal conductivities along with the film-substrate TBR of the heterostructure are fitted. In virtue of the three-sensor  $3\omega$ - $2\omega$  method, two typical wide bandgap semiconductor heterostructure samples, i.e., GaN on SiC (#SiC)

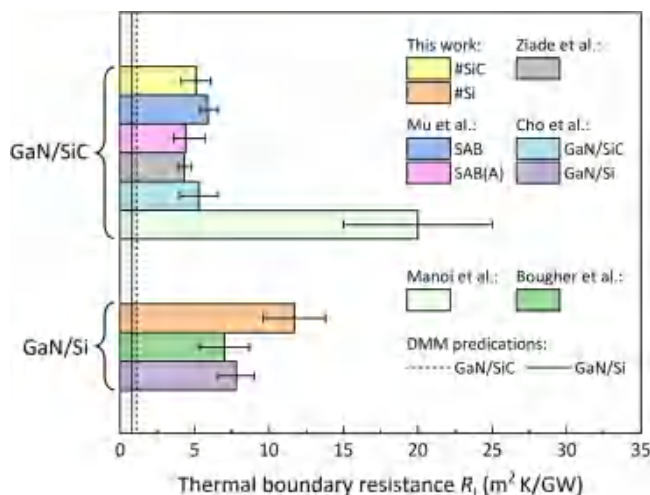


FIG. 7. Comparison of TBR results in this study with representative studies in the literature (300 K).

and GaN on Si (#Si) with GaN layer thicknesses of  $\sim 2.3\ \mu\text{m}$ , are measured. The thermal conductivity of the GaN films, the thermal conductivity of the SiC and Si substrates, and the TBRs between the GaN and substrates are all consistent with the representative results in the literature, verifying the reliability and accuracy of the method. This method will provide a comprehensive solution for the demands of thermophysical property measurements of various solid heterostructures.

#### SUPPLEMENTARY MATERIAL

See the [supplementary material](#) for the comparison between the three-sensor  $3\omega$ - $2\omega$  method and the previous two-sensor  $3\omega$ - $2\omega$  method (Sec. S1), the four-parameter fitting procedure (Sec. S2), the sensitivity analysis of typical GaN on SiC heterostructures, the resulting feasible regions for the three-sensor layout design (Sec. S3), the sensitivity analysis of other three kinds of typical heterostructures (GaN on Si,  $\text{Ga}_2\text{O}_3$  on SiC, and  $\text{aAl}_2\text{O}_3$  on Si) (Sec. S4), the measurement details of the sensors' dimensions (Sec. S5), the measurement details of the sensors' TCRs (Sec. S6), and the error analysis (Sec. S7).

#### ACKNOWLEDGMENTS

This work was financially supported by the National Natural Science Foundation of China (NNSFC) (Grant Nos. 51825601 and U20A20301).

#### AUTHOR DECLARATIONS

Conflict of interest

The authors have no conflicts to disclose.

#### Author Contributions

Guang Yang: Conceptualization (lead); Data curation (lead); Formal analysis (lead); Investigation (lead); Methodology (lead); Resources (supporting); Software (lead); Validation (lead); Visualization (lead); Writing – original draft (lead). Bing-yang Cao: Conceptualization (supporting); Funding acquisition (lead); Project administration (lead); Resources (lead); Supervision (lead); Writing – review & editing (lead).

#### DATA AVAILABILITY

The data that support the findings of this study are available from the corresponding author upon reasonable request.

#### REFERENCES

- <sup>1</sup>Z. I. Alferov, "Nobel lecture: The double heterostructure concept and its applications in physics, electronics, and technology," *Rev. Mod. Phys.* 73(3), 767 (2001).
- <sup>2</sup>H. Kressel, "Materials for heterojunction devices," *Annu. Rev. Mater. Sci.* 10(1), 287 (1980).
- <sup>3</sup>K. Yau, E. Dacquay, I. Sarkas, and S. P. Voinigescu, "Device and IC characterization above 100 GHz," *IEEE Microw. Mag.* 13(1), 30 (2012).
- <sup>4</sup>S. J. Pearton and F. Ren, "GaN electronics," *Adv. Mater.* 12(21), 1571 (2000).
- <sup>5</sup>A. J. Green, J. Speck, G. Xing, P. Moens, F. Allerstam, K. Gumaelius, T. Neyer, A. Arias-Purdue, V. Mehrotra, A. Kuramata, K. Sasaki, S. Watanabe, K. Koshi,

J. Blevins, O. Bierwagen, S. Krishnamoorthy, K. Leedy, A. R. Arehart, A. T. Neal, S. Mou, S. A. Ringel, A. Kumar, A. Sharma, K. Ghosh, U. Singiseti, W. Li, K. Chabak, K. Liddy, A. Islam, S. Rajan, S. Graham, S. Choi, Z. Cheng, and M. Higashiwaki, " $\beta$ -gallium oxide power electronics," *APL Mater.* 10(2), 029201 (2022).

<sup>6</sup>A. J. Heeger, "25th anniversary article: Bulk heterojunction solar cells: Understanding the mechanism of operation," *Adv. Mater.* 26(1), 10 (2014).

<sup>7</sup>J. Chen, W. Ouyang, W. Yang, J.-H. He, and X. Fang, "Recent progress of hetero-junction ultraviolet photodetectors: Materials, integrations, and applications," *Adv. Funct. Mater.* 30(16), 1909909 (2020).

<sup>8</sup>D. M. Rowe, "Recent developments in thermoelectric materials," *Appl. Energy* 24(2), 139 (1986).

<sup>9</sup>A. Bar-Cohen, J. D. Albrecht, and J. J. Maurer, "Near-junction thermal management for wide bandgap devices," in 2011 IEEE Compound Semiconductor Integrated Circuit Symposium (CSICS), 16–19 October 2011 (Curran Associates, Waikoloa, Hawaii, 2011).

<sup>10</sup>Z. Cheng, S. Graham, H. Amano, and D. G. Cahill, "Perspective on thermal conductance across heterogeneously integrated interfaces for wide and ultrawide bandgap electronics," *Appl. Phys. Lett.* 120(3), 030501 (2022).

<sup>11</sup>Y. Won, J. Cho, D. Agonafer, M. Asheghi, and K. E. Goodson, "Cooling limits for GaN HEMT technology," in 2013 IEEE Compound Semiconductor Integrated Circuit Symposium (CSICS), 13–16 October 2013 (Curran Associates, Monterey, CA, 2013).

<sup>12</sup>Y. Won, J. Cho, D. Agonafer, M. Asheghi, and K. E. Goodson, "Fundamental cooling limits for high power density gallium nitride electronics," *IEEE Trans. Compon. Packag. Manuf. Technol.* 5(6), 737 (2015).

<sup>13</sup>R. J. Warzoha, A. A. Wilson, B. F. Donovan, N. Donmezer, A. Giri, P. E. Hopkins, S. Choi, D. Pahinkar, J. Shi, S. Graham, Z. Tian, and L. Ruppalt, "Applications and impacts of nanoscale thermal transport in electronics packaging," *J. Electron. Packag.* 143(2), 020804 (2021).

<sup>14</sup>P. Jiang, X. Qian, and R. Yang, "Tutorial: Time-domain thermoreflectance (TDTR) for thermal property characterization of bulk and thin film materials," *J. Appl. Phys.* 124(16), 161103 (2018).

<sup>15</sup>A. J. Schmidt, R. Cheaito, and M. Chiesa, "A frequency-domain thermoreflectance method for the characterization of thermal properties," *Rev. Sci. Instrum.* 80(9), 094901 (2009).

<sup>16</sup>Z. Cheng, F. Mu, T. You, W. Xu, J. Shi, M. E. Liao, Y. Wang, K. Huynh, T. Suga, M. S. Goorsky, X. Ou, and S. Graham, "Thermal transport across Ion-Cut monocrystalline  $\beta$ - $\text{Ga}_2\text{O}_3$  thin films and bonded  $\beta$ - $\text{Ga}_2\text{O}_3$ -SiC interfaces," *ACS Appl. Mater. Interfaces* 12(40), 44943 (2020).

<sup>17</sup>J. L. Braun, D. H. Olson, J. T. Gaskins, and P. E. Hopkins, "A steady-state thermoreflectance method to measure thermal conductivity," *Rev. Sci. Instrum.* 90(2), 024905 (2019).

<sup>18</sup>Y. Song, D. Shoemaker, J. H. Leach, C. McGray, H.-L. Huang, A. Bhattacharyya, Y. Zhang, C. U. Gonzalez-Valle, T. Hess, S. Zhukovsky, K. Ferri, R. M. Lavelle, C. Perez, D. W. Snyder, J.-P. Maria, B. Ramos-Alvarado, X. Wang, S. Krishnamoorthy, J. Hwang, B. M. Foley, and S. Choi, " $\text{Ga}_2\text{O}_3$ -on-SiC composite wafer for thermal management of ultrawide bandgap electronics," *ACS Appl. Mater. Interfaces* 13(34), 40817 (2021).

<sup>19</sup>A. Sarua, H. Ji, K. P. Hilton, D. J. Wallis, M. J. Uren, T. Martin, and M. Kuball, "Thermal boundary resistance between GaN and substrate in AlGaIn/GaN electronic devices," *IEEE Trans. Electron Devices* 54(12), 3152 (2007).

<sup>20</sup>R. J. T. Simms, J. W. Pomeroy, M. J. Uren, T. Martin, and M. Kuball, "Channel temperature determination in high-power AlGaIn/GaN HFETs using electrical methods and Raman spectroscopy," *IEEE Trans. Electron Devices* 55(2), 478 (2008).

<sup>21</sup>M. Kuball and J. W. Pomeroy, "A review of Raman thermography for electronic and opto-electronic device measurement With submicron spatial and nanosecond temporal resolution," *IEEE Trans. Device Mater. Reliab.* 16(4), 667 (2016).

<sup>22</sup>J. Cho, L. Zijian, M. Asheghi, and K. Goodson, "Near-junction thermal management: Thermal conduction in gallium nitride composite substrates," *Annu. Rev. Heat Transfer* 18, 7–45 (2015).

- <sup>23</sup>J. Martan, J. Čapek, and E. A. Chalhoub, "Measurement of thermal properties of thin films up to high temperatures—pulsed photothermal radiometry system and Si–B–C–N films," *Rev. Sci. Instrum.* 81(12), 124902 (2010).
- <sup>24</sup>J. Zeng, K. M. Chung, Q. Wang, X. Wang, Y. Pei, P. Li, and R. Chen, "Measurement of high-temperature thermophysical properties of bulk and coatings using modulated photothermal radiometry," *Int. J. Heat Mass Transfer* 170, 120989 (2021).
- <sup>25</sup>J. Zeng, K. M. Chung, S. R. Adapa, T. Feng, and R. Chen, "In-situ thermal transport measurement of flowing fluid using modulated photothermal radiometry," *Int. J. Heat Mass Transfer* 180, 121767 (2021).
- <sup>26</sup>N. Horny, M. Chirtoc, A. Fleming, G. Hamaoui, and H. Ban, "Kapitza thermal resistance studied by high-frequency photothermal radiometry," *Appl. Phys. Lett.* 109(3), 033103 (2016).
- <sup>27</sup>P. Kijamnajsuk, F. Giuliani, M. Chirtoc, N. Horny, J. Gibkes, S. Chotikaprakhan, B. K. Bein, and J. Pelzl, "Interface resistance in copper coated carbon determined by frequency dependent photothermal radiometry," *J. Phys.: Conf. Ser.* 214(1), 012053 (2010).
- <sup>28</sup>E. T. Swartz and R. O. Pohl, "Thermal resistance at interfaces," *Appl. Phys. Lett.* 51(26), 2200 (1987).
- <sup>29</sup>C. Dames, "Measuring the thermal conductivity of thin films: 3 omega and related electrothermal methods," *Annu. Rev. Heat Transfer* 16, 7–49 (2013).
- <sup>30</sup>H.-S. Yang, J. W. Kim, G. H. Park, C. S. Kim, K. Kyhm, S. R. Kim, K. C. Kim, and K. S. Hong, "Interfacial effect on thermal conductivity of Y2O3 thin films deposited on Al2O3," *Thermochim. Acta* 455(1), 50 (2007).
- <sup>31</sup>S. Deng, C. Xiao, J. Yuan, D. Ma, J. Li, N. Yang, and H. He, "Thermal boundary resistance measurement and analysis across SiC/SiO2 interface," *Appl. Phys. Lett.* 115(10), 101603 (2019).
- <sup>32</sup>Y.-C. Hua and B.-Y. Cao, "A two-sensor 3ω-2ω method for thermal boundary resistance measurement," *J. Appl. Phys.* 129(12), 125107 (2021).
- <sup>33</sup>Y. Zhang, W. Zhu, F. Hui, M. Lanza, T. Borca-Tasciuc, and M. Muñoz Rojo, "A review on principles and applications of scanning thermal microscopy (SThM)," *Adv. Funct. Mater.* 30(18), 1900892 (2020).
- <sup>34</sup>S. Gomès, L. David, V. Lysenko, A. Descamps, T. Nychporuk, and M. Raynaud, "Application of scanning thermal microscopy for thermal conductivity measurements on meso-porous silicon thin films," *J. Phys. D: Appl. Phys.* 40(21), 6677 (2007).
- <sup>35</sup>S. Gomès, P. Newby, B. Canut, K. Termentzidis, O. Marty, L. Fréchette, P. Chantrenne, V. Aimez, J.-M. Bluet, and V. Lysenko, "Characterization of the thermal conductivity of insulating thin films by scanning thermal microscopy," *Microelectron. J.* 44(11), 1029 (2013).
- <sup>36</sup>G. Chen, "Non-Fourier phonon heat conduction at the microscale and nanoscale," *Nat. Rev. Phys.* 3(8), 555 (2021).
- <sup>37</sup>D. G. Cahill, "Thermal conductivity measurement from 30 to 750 K: The 3ω method," *Rev. Sci. Instrum.* 61(2), 802 (1990).
- <sup>38</sup>D. G. Cahill and R. O. Pohl, "Thermal conductivity of amorphous solids above the plateau," *Phys. Rev. B* 35(8), 4067 (1987).
- <sup>39</sup>C. Chiritescu, D. G. Cahill, N. Nguyen, D. Johnson, A. Bodapati, P. Koblinski, and P. Zschack, "Ultralow thermal conductivity in disordered, layered WSe2 crystals," *Science* 315(5810), 351 (2007).
- <sup>40</sup>C. E. Raudzis, F. Schatz, and D. Wharam, "Extending the 3ω method for thin-film analysis to high frequencies," *J. Appl. Phys.* 93(10), 6050 (2003).
- <sup>41</sup>Y. Liu, J. Qiu, L. Liu, and B. Cao, "Extracting optical constants of solid materials with micro-rough surfaces from ellipsometry without using effective medium approximation," *Opt. Express* 27(13), 17667 (2019).
- <sup>42</sup>C. Dames and G. Chen, "1ω, 2ω, and 3ω methods for measurements of thermal properties," *Rev. Sci. Instrum.* 76(12), 124902 (2005).
- <sup>43</sup>B. W. Olson, S. Graham, and K. Chen, "A practical extension of the 3ω method to multilayer structures," *Rev. Sci. Instrum.* 76(5), 053901 (2005).
- <sup>44</sup>A. Bedoya, J. Jaime, F. Rodríguez-Valdés, C. García-Segundo, A. Calderón, R. Ivanov, and E. Marin, "Thermal impedance," *Eur. J. Phys.* 42(6), 065101 (2021).
- <sup>45</sup>M. Handweg, R. Mitdank, Z. Galazka, and S. F. Fischer, "Temperature-dependent thermal conductivity and diffusivity of a Mg-doped insulating β-Ga2O3 single crystal along [100], [010] and [001]," *Semicond. Sci. Technol.* 31(12), 125006 (2016).
- <sup>46</sup>R. L. Xu, M. Muñoz Rojo, S. M. Islam, A. Sood, B. Vareskic, A. Katre, N. Mingo, K. E. Goodson, H. G. Xing, D. Jena, and E. Pop, "Thermal conductivity of crystalline AlN and the influence of atomic-scale defects," *J. Appl. Phys.* 126(18), 185105 (2019).
- <sup>47</sup>D. Zhao, X. Qian, X. Gu, S. A. Jajja, and R. Yang, "Measurement techniques for thermal conductivity and interfacial thermal conductance of bulk and thin film materials," *J. Electron. Packag.* 138(4), 040802 (2016).
- <sup>48</sup>A. T. Ramu and J. E. Bowers, "A '2-omega' technique for measuring anisotropy of thermal conductivity," *Rev. Sci. Instrum.* 83(12), 124903 (2012).
- <sup>49</sup>J. Cho, Y. Li, W. E. Hoke, D. H. Altman, M. Asheghi, and K. E. Goodson, "Phonon scattering in strained transition layers for GaN heteroepitaxy," *Phys. Rev. B* 89(11), 115301 (2014).
- <sup>50</sup>J. Cho, Y. Li, D. H. Altman, W. E. Hoke, M. Asheghi, and K. E. Goodson, "Temperature dependent thermal resistances at GaN-substrate interfaces in GaN composite substrates," in 2012 IEEE Compound Semiconductor Integrated Circuit Symposium (CSICS), 14–17 October 2012 (Curran Associates, La Jolla, CA, 2012).
- <sup>51</sup>C. Y. Luo, H. Marchand, D. R. Clarke, and S. P. DenBaars, "Thermal conductivity of lateral epitaxial overgrown GaN films," *Appl. Phys. Lett.* 75(26), 4151 (1999).
- <sup>52</sup>T. L. Bougher, L. Yates, C.-F. Lo, W. Johnson, S. Graham, and B. A. Cola, "Thermal boundary resistance in GaN films measured by time domain thermoreflectance with robust monte carlo uncertainty estimation," *Nanoscale Microscale Thermophys. Eng.* 20(1), 22 (2016).
- <sup>53</sup>E. Ziade, J. Yang, G. Brummer, D. Nothert, T. Moustakas, and A. J. Schmidt, "Thermal transport through GaN–SiC interfaces from 300 to 600 K," *Appl. Phys. Lett.* 107(9), 091605 (2015).
- <sup>54</sup>F. Mu, Z. Cheng, J. Shi, S. Shin, B. Xu, J. Shiomi, S. Graham, and T. Suga, "High thermal boundary conductance across bonded heterogeneous GaN–SiC interfaces," *ACS Appl. Mater. Interfaces* 11(36), 33428 (2019).
- <sup>55</sup>Y. Zhao, C. Zhu, S. Wang, J. Z. Tian, D. J. Yang, C. K. Chen, H. Cheng, and P. Hing, "Pulsed photothermal reflectance measurement of the thermal conductivity of sputtered aluminum nitride thin films," *J. Appl. Phys.* 96(8), 4563 (2004).
- <sup>56</sup>A. Manoi, J. W. Pomeroy, N. Killat, and M. Kuball, "Benchmarking of thermal boundary resistance in AlGaIn/GaN HEMTs on SiC substrates: Implications of the nucleation layer microstructure," *IEEE Electron Device Lett.* 31(12), 1395 (2010).
- <sup>57</sup>Y.-H. Li, R.-S. Qi, R.-C. Shi, J.-N. Hu, Z.-T. Liu, Y.-W. Sun, M.-Q. Li, N. Li, C.-L. Song, L. Wang, Z.-B. Hao, Y. Luo, Q.-K. Xue, X.-C. Ma, and P. Gao, "Atomic-scale probing of heterointerface phonon bridges in nitride semiconductor," *Proc. Natl. Acad. Sci. U.S.A.* 119(8), e2117027119 (2022).
- <sup>58</sup>J. Hu, Z. Hao, L. Niu, E. Yanxiong, L. Wang, and Y. Luo, "Atomically smooth and homogeneously N-polar AlN film grown on silicon by aluminization of Si3N4," *Appl. Phys. Lett.* 102(14), 141913 (2013).
- <sup>59</sup>S. Zhang, Y. Zhang, Y. Cui, C. Freysoldt, J. Neugebauer, R. R. Lieten, J. S. Barnard, and C. J. Humphreys, "Interfacial structure and chemistry of GaN on Ge(111)," *Phys. Rev. Lett.* 111(25), 256101 (2013).
- <sup>60</sup>A. Giri and P. E. Hopkins, "A review of experimental and computational advances in thermal boundary conductance and nanoscale thermal transport across solid interfaces," *Adv. Funct. Mater.* 30(8), 1903857 (2020).